Mathematical modelling of the restenosis process after stent implantation

Javier Escuer[1] · **Miguel A. Martínez**[1,2] · **Sean McGinty**[3] · **Estefanía Peña**[1,2]

Abstract The stenting procedure has evolved to become a highly successful technique for the clinical treatment of advanced atherosclerotic lesions in arteries. However, the development of in-stent restenosis remains a key problem. In this work, a novel 2D continuum mathematical model is proposed to describe the complex restenosis process following the insertion of a stent into a coronary artery. The biological species considered to play a key role in restenosis development are growth factors, matrix metalloproteinases, extracellular matrix, smooth muscle cells and endothelial cells. Diffusion-reaction equations are utilized for modelling the mass balance between species in the arterial wall. Experimental data from the literature have been used in order to estimate model parameters. Moreover, a sensitivity analysis has been performed to study the impact of varying the parameters of the model on the evolution of the biological species. The results demonstrate that this computational model qualitatively captures the key characteristics of the lesion growth and the healing process within an artery subjected to non-physiological mechanical forces. Our results suggest that the arterial wall response is driven by the damage area, smooth muscle cells proliferation and the collagen turnover among other factors.

Keywords: restenosis, stent, ISR, coronary artery, diffusion-reaction equations, continuum models.

1 Introduction

Cardiovascular diseases (CVDs) are the leading cause of mortality in the world. In Europe, 3.9 million deaths a year are attributed to CVDs, with coronary heart disease (CHD) and stroke the primary culprits [1]. CHD is characterized by the development of atherosclerotic plaque, consisting of deposits of cholesterol and other lipids, calcium and macrophages, within the arterial wall. This causes a progressive reduction in the lumen available for the blood flow (stenosis), hardening and loss of elasticity of the arterial tissue.

[1]Applied Mechanics and Bioengineering Group (AMB), Aragón Institute of Engineering Research (I3A), University of Zaragoza, Zaragoza, Spain.
[2]Biomedical Research Networking Center in Bioengineering, Biomaterials and Nanomedicine (CIBER-BBN), Spain.
[3]Division of Biomedical Engineering, University of Glasgow, Glasgow, UK.

The use of endovascular devices such as stents and balloons to treat advanced atherosclerotic lesions is now commonplace in the clinic. However, one of the major limitations of these interventions is the development of restenosis [2–7]. Restenosis is understood to comprise of three main mechanisms: elastic recoil (in the short term), vessel remodelling and neointimal hyperplasia (in the longer term). The first and second mechanisms are typical in the case of balloon angioplasty, whereas stent deployment usually promotes the formation of neointimal hyperplasia, associated with smooth muscle cell (SMC) migration and proliferation and extracellular matrix (ECM) deposition [7]. Coronary revascularization now generally involves the use of a stent in more than 70% of cases, leading to reduced restenosis rates in comparison to balloon angioplasty alone. With the advent of drug-eluting stents (DES) the incidence of restenosis has been dramatically reduced to approximately $<$10-12% of all angioplasties [8]. However, DES do not completely remove this problem. Since the precise mechanisms behind restenosis after stenting, so-called in-stent restenosis (ISR), are still not fully understood, it therefore remains a significant clinical challenge to predict which patients will develop ISR.

Experimental studies have established a strong correlation between the level of arterial injury caused by the device and the following neointimal thickness and lumen diameter reduction at the stented area [9, 10]. Novel stent designs and stent-deployment protocols that minimise induced vascular injury are therefore needed. However, the optimum stent design and the ideal drug release strategy still remain in question despite technological advances [11].

Complementary to the wide variety of experimental studies, computational analysis has emerged as a useful method for designing new medical devices in order to minimise ISR. In the last two decades, many computational models of stent deployment have been developed to study the stress-strain level that the device induces within the arterial wall [12–15]. Several mathematical and numerical models have also been developed to try to understand drug release from stents and subsequent redistribution in the arterial tissue [16–20]. Less attention, however, has been directed to modelling the biological response to treatment.

In recent years, mechanobiological models have emerged to relate mechanics to the complex biological response. These have primarily made use of discrete agent based models (ABM) or cellular automata (CA) methods, in some cases combining with finite element analysis (FEA). For example, Zahedmanesh et al. developed an agent based model to investigate the dynamics of the SMC in vascular tissue engineering scaffolds [21] and an ABM of ISR which allows a quantitative evaluation of the ECM turnover after stent-induced vascular injury [22]; Boyle et al. demonstrated that non-linear growth could be simulated with a cell-centred model [23] and simulated ISR by modelling a combination of injury and inflammation with SMCs represented as discrete agents [24, 25] and; Keshavarzian et al. [26] developed a mechanobiological model of arterial growth and remodelling. Evans et al. [27] highlighted the importance of using a multiscale approach to describe computationally the main physical and biological processes implicated in ISR, introducing the concept of the complex autonoma (CxA) models, based on a hierarchical aggregation of coupled CA and ABM models. Tahir et al. [28] focussed on the initial phase after stenting and developed a cellular Potts model from which they hypothesized that deeper stent deployment allows easier migration of SMC into the lumen. Most recently, Zun et al. [29] presented a 3D multiscale model of ISR with blood flow simulations coupled to an agent-based SMC proliferation model and demonstrated qualitative agreement with *in vivo* porcine data. In the aforementioned examples, discrete

models attempted to represent individual cells in the form of a lattice governed by a set of rules, in contrast to the continuum approach where the evolution of populations of cells and other species such as growth factors are described through partial differential equations (PDEs).

In terms of continuum models, Rachev et al. [30] proposed a theoretical continuum model to describe the main mechanisms of the coupled deformation and stress-induced arterial tissue thickening observed at the regions close to an implanted stent, comparing the results obtained with experimental data documented in the available literature [31]. However, this phenomenological model does not take into account, for example, the mechanisms implicated in the SMC proliferation or the ECM synthesis. Other continuum mathematical biological models typically comprise of a series of coupled diffusion-reaction equations for describing the biological interaction between several species. Such models have been developed to describe phenomena such as neointimal hyperplasia formation [32], atherosclerotic plaque formation [33–36], fibrotic tissue formation surrounding medical implants [37, 38] and more recently, in-stent restenosis [39] and arterial physiopathology [40]. In contrast to discrete models where cell behaviour is usually described by a set of rules, continuum models offer a mechanistic description, featuring physical parameters which may in principle be measured. In addition, continuum models often have a lower computational cost than ABM, and naturally allow for modelling diffusion of species and coupling with the mechanical aspects of the problem.

In this paper, we develop a model that allows us to simulate the restenosis process following the insertion of a stent into a coronary artery. The key novelty of our model is that it adopts a continuum approach to describe the sequence of events following damage to the arterial wall, and is therefore formulated in terms of densities/concentrations of a number of important species. This is advantageous because it allows us to assess how the evolution of the various species affects the overall healing process, and more importantly, how variations in the associated parameters and initial conditions influences the process. Diffusion-reaction equations are used for modelling the mass balance between biological species in the arterial wall. The main species considered to play a key role in the process are SMCs, endothelial cells (ECs), matrix-degrading metalloproteinases (MMPs), growth factors (GFs) and ECM. The parameters used in the model to define the biological interaction between the different species have been adapted from experimental data available in the literature. Unlike any of the existing continuum models, we are able to simulate the time-course response of six different biological species involved in ISR after the initial mechanical damage, whilst at the same time simulating tissue growth. Our primary aim is to gain insight into the physical mechanisms of tissue remodelling post-stenting. Simulating patient-specific cases is beyond the scope of this work: historically, mathematical and computational models in the stents domain have been formulated in idealised scenarios to gain insight before moving onto more realistic patient-specific geometries. With this in mind, we employ a simplified geometry. Notwithstanding, we do compare our results to clinical data and use our model to asses the impact of geometric variations on the final outcome through consideration of a series of commercial stents as well as different inter-strut distances and levels of strut embedment, thereby enabling us to relate our findings to stent design.

2 Governing equations and model assumptions

ISR is an immeasurably complex multiscale system involving a large number of species and an intricate cascade of biological processes (Fig. 1). Indeed, much of the biology is still unknown. Due to its complexity, in this model we include only what we believe are the predominant species and processes. Specifically, we consider three types of cells (contractile and synthetic SMCs and ECs) and three extracellular components (GFs, MMPs and ECM). We consider the following behaviour: cell types can proliferate, migrate, differentiate and die (apoptosis) while the extracellular components can be produced or degraded. Since the processes considered take place predominantly in the intima and media layers, in the following model the arterial wall refers to these layers, with the adventitia considered as the outer boundary. Furthermore, blood flow in the lumen and plasma filtration in the tissue have not been included. We refer the reader to Section 5 for a full discussion of the limitations of this work.

[Fig. 1 about here.]

2.1 Material model

An isotropic hyperelastic constitutive model based on a Yeoh strain energy function (SEF) [41] was considered to describe the stress-strain response of the arterial wall. We assume the same mechanical response for the intima and the media layer. Assuming incompressibility of the tissue, the Yeoh SEF can be written as:

$$\Psi = c_{10}(I_1 - 3) + c_{20}(I_1 - 3)^2 + c_{30}(I_1 - 3)^2 \tag{1}$$

where $c_{10} = 17.01$ kPa, $c_{20} = -73.42$ kPa and $c_{30} = 414.95$ kPa, are the hyperelastic material constants and I_1 is the first strain invariant of the Cauchy-Green deformation tensor. The coefficients of the hyperelastic model were identified from fitting the experimental results obtained from Holzapfel et al. [42] in specimens of human coronary arteries for the media layer in the circumferential direction using the software for calibration of hyperelastic material models (HyperFit, www.hyperfit.wz.cz).
The stent is modelled as an elasto-plastic material with a Young's modulus of E=200 GPa, Poisson's ratio of ν =0.28 (representative of biomedical grade stainless steel alloy 316L) and plasticity described by isotropic hardening J_2 flow theory with the tensile stress-strain curves taken from the literature, including a yield strength of 264 MPa and a ultimate tensile strength (UTS) of 584 MPa at an engineering plastic strain of 0.247 [15].

2.2 Initial estimation and evolution of the damage

Although not completely elucidated, the stimulus triggering the cascade of inflammatory events leading to neointimal formation appears to come from the endothelial damage caused immediately after balloon dilatation and stent placement [43]. We do not explicitly account for all of the mechanical factors that initiate the process which leads to vessel injury and endothelial dysfunction. Following Zahedmanesh et al. [22], we assign a level of injury to the arterial wall, d, in a continuous range from 0 to 1. Due to the absence of reliable mechanical data in literature on the stress-strain levels known to

cause arterial injury, the experimental data of *in vitro* tensile tests up to failure of 13 human left anterior descending (LAD) coronary arteries [42] were used to obtain a qualitative estimation of the damage in the tissue. In particular, we define a piecewise linear function to prescribe the initial arterial damage as a function of von Mises stress, σ_{vm}, calculated by a FE simulation of the stent expansion:

$$d_0 = \begin{cases} 0 & if \quad \sigma_{vm} \leq \sigma_{vm,inf} \\ \frac{\sigma_{vm}-\sigma_{vm,inf}}{\sigma_{vm,sup}-\sigma_{vm,inf}} & if \ \sigma_{vm,inf} < \sigma_{vm} < \sigma_{vm,sup} \\ 1 & if \quad \sigma_{vm} \geq \sigma_{vm,sup} \end{cases} \tag{2}$$

where d_0 is the initial damage in the tissue due to the stent placement. This function assigns a value of zero for the damage in areas of the arterial wall in which von Mises stress is lower than $\sigma_{vm,inf}$ and a value of 1 for the damage in those regions in which von Mises stress exceed $\sigma_{vm,sup}$ (Fig. 2).

[Fig. 2 about here.]

Moreover, damage, d, is assumed to decrease continuously with time at a rate directly proportional to the MMP concentration, c_{mmp} [24]. The damage evolution equation is therefore:

$$\frac{\partial d}{\partial t} = \underbrace{-k_{deg,d}\ d\ c_{mmp}}_{\text{Degradation}}, \tag{3}$$

where d is a continuous function of space and time, $d(r,z,t)$, to describe the damage level, $k_{deg,d}$ is the degradation rate of damage and $c_{mmp}(r,z,t)$ is the concentration of MMP. Eq. 3 may be considered as a simple description of healing.

2.3 Species evolution

(a) Growth Factors (GFs):

After mechanical arterial injury, platelets, leukocytes and SMCs, among others, release several types of GFs: platelet-derived GF (PDGF), epidermal GF (EGF), insulin-like GF (IGF), transforming GF (TGF) and fibroblast GF (FGF) [2, 3, 5, 7]. However, since their specific roles in the inflammatory phase are not completely understood [2], the term GF includes the combined action of all of them. Denoting the concentration of GFs in the arterial wall by $c_{gf}(r,z,t)$, and assuming an initial value of $c_{gf,0}$ [44], their behaviour is modeled as follows:

$$\frac{\partial c_{gf}}{\partial t} + \underbrace{\nabla \cdot (-D_{gf} \nabla c_{gf})}_{\text{Random motion}} = \underbrace{k_{prod,gf}\ d \left(1 - \frac{c_{gf}}{c_{gf,th}}\right)}_{\text{Production}} - \underbrace{k_{deg,gf}\left(c_{gf} - c_{gf,0}\right)}_{\text{Degradation}}. \tag{4}$$

We are assuming that the GFs experience random motion (i.e., diffusion). Although the diffusion coefficient, D_{gf}, may in general depend on position, we take it here to be constant [32]. The right hand side of Eq. 4 considers a dynamic balance between degradation

and production. GF production is assumed to follow logistic growth: the concentration increases proportionally to the production rate, $k_{prod,gf}$, and level of damage, d, until some threshold value, $c_{gf,th}$, is reached. To simplify the mathematical model, we consider that vascular damage is the only trigger of GF production. Degradation, on the other hand, is assumed to occur at a constant rate, $k_{deg,gf}$, and in proportion to the 'distance' from the initial value.

(b) Matrix-degrading metalloproteinases (MMPs):

Human MMPs are a family of 26 members of zinc-dependent proteolytic enzymes which are considered to be the normal and physiologically relevant mediators of ECM degradation [45, 46]. Given that MMP-2 cleaves a wider range of ECM constituents [22], the term MMP specifically refers to MMP-2 in this model. ECs, SMCs, fibroblasts and infiltrating inflammatory cells are able to produce MMPs. In this work, we assume that mechanical damage resulting from stenting upregulates MMP production only by SMCs [46], while at the same time MMP is reduced at a constant rate [24]. The MMP evolution equation is defined as follows:

$$\frac{\partial c_{mmp}}{\partial t} + \underbrace{\nabla \cdot (-D_{mmp} \nabla c_{mmp})}_{\text{Random motion}} = \underbrace{\left(k_{prod1,mmp} c_{csmc} + k_{prod2,mmp} c_{ssmc}\right) d \left(1 - \frac{c_{mmp}}{c_{mmp,th}}\right)}_{\text{Production}} - \underbrace{k_{deg,mmp} \left(c_{mmp} - c_{mmp,0}\right)}_{\text{Degradation}}, \quad (5)$$

where c_{mmp} is the concentration of MMPs, D_{mmp} is the diffusion coefficient to simulate the random movement of MMP molecules, $k_{prod1,mmp}$ and $k_{prod2,mmp}$ are the production rates of MMPs by contractile and synthetic SMCs, respectively, and $k_{deg,mmp}$ is the constant degradation rate of MMPs. The parameter $c_{mmp,0}$ represents the initial concentration of MMP in the tissue [47], whilst $c_{mmp,th}$ is the threshold MMP concentration.

(c) Extracellular Matrix (ECM)

The ECM is the non-cellular component of the arterial wall that provides physical scaffolding for the cellular constituents and is responsible for cell-matrix interactions [48], playing a crucial role in the development of the pathogenesis of restenosis. In particular, ECM components are involved in the regulation of SMCs phenotype: degradation of ECM after stenting promotes the transition of SMCs from a quiescent/contractile to an active/synthetic phenotype, whereas its synthesis leads to the opposite [49]. In this work, the behaviour of ECM has been directly related to the behaviour of collagen which constitutes the major component of mature restenotic tissue [7]. For this reason, collagen is assumed to be the only component of the ECM in our model. Collagen is secreted by synthetic SMCs [2] and degraded at a rate proportional to the amount of MMPs [7, 24], so its behaviour can be defined as follows:

$$\frac{\partial c_{ecm}}{\partial t} = \underbrace{k_{prod,ecm} c_{ssmc} \left(1 - \frac{c_{ecm}}{c_{ecm,th1}}\right)}_{\text{Production}} - \underbrace{k_{deg,ecm} \left(c_{mmp} - c_{mmp,0}\right) \left(1 - \frac{c_{ecm,th2}}{c_{ecm}}\right)}_{\text{Degradation}}, \quad (6)$$

where $c_{ecm}(r, z, t)$ is the concentration of collagen, which is produced at a rate $k_{prod,ecm}$ and degraded at a degradation rate $k_{deg,ecm}$. The initial concentration of collagen is $c_{ecm,0}$ [47]. We assume that the natural synthesis of collagen is equal to the age-related degradation rate, therefore these terms have not been taken into account in this equation. Moreover, we assume that ECM kinetics are dominated by production and degradation and that random motion of ECM is negligible.

(d) Contractile smooth muscle cells (cSMC)

SMCs are the most prominent cell type found in intimal hyperplasia. In our model, SMCs can exist in one of two phenotypes: contractile or synthetic. Before stent implantation, SMCs are in a quiescent/contractile phenotype (do not proliferate or synthesize matrix) within the uninjured tissue. We can define the behaviour of the contractile SMCs as:

$$\frac{\partial c_{csmc}}{\partial t} = \underbrace{-k_{diff,csmc} c_{csmc} K_{ssmc,ecm}}_{\substack{\text{Differentiation} \\ \text{from cSMC to sSMC}}} + \underbrace{k_{diff,ssmc} c_{ssmc} K_{csmc,ecm}}_{\substack{\text{Differentiation} \\ \text{from sSMC to cSMC}}}, \quad (7)$$

where $c_{csmc}(r, z, t)$ is the contractile SMCs concentration, $k_{diff,csmc}$ is the differentation rate from contractile SMCs to synthetic SMCs, $k_{diff,ssmc}$ is the differentation rate from synthetic SMCs to contractile SMCs and $K_{cSMC,ecm}$ and $K_{ssmc,ecm}$ (Fig. 3) are functions defined to modulate the SMCs differentiation as a function of the ECM concentration:

$$K_{ssmc,ecm} = -\left(e^{-\left(\frac{c_{ecm,th}}{c_{ecm}} - 1\right) - \left|\frac{c_{ecm,th}}{c_{ecm}} - 1\right|} - 1\right), \quad (8)$$

$$K_{csmc,ecm} = -\left(e^{-\left(\frac{c_{ecm}}{c_{ecm,th}} - 1\right) - \left|\frac{c_{ecm}}{c_{ecm,th}} - 1\right|} - 1\right). \quad (9)$$

In this model, contractile SMCs may differentiate into synthetic SMCs and vice-versa. The function $K_{ssmc,ecm}$ contributes to the emergence of the synthetic phenotype, so when $c_{ecm} < c_{ecm,th}$ the function $K_{ssmc,ecm}$ takes positives values, SMCs are activated and switch to a synthetic phenotype starting to migrate, proliferate and synthesize ECM, while if $c_{ecm} \geqslant c_{ecm,th}$ then $K_{ssmc,ecm}$ is equal to zero (no differentiation). On the other hand, $K_{csmc,ecm}$ contributes to the emergence of the contractile phenotype, so when $c_{ecm} \leqslant c_{ecm,th}$ then $K_{csmc,ecm}$ is zero and if $c_{ecm} > c_{ecm,th}$ the function $K_{csmc,ecm}$ takes a positive value and synthetic SMCs switch back to the contractile phenotype. At the beginning of the simulation $c_{ecm} = c_{ecm,th}$ so $K_{ssmc,ecm}$

and $K_{csmc,ecm}$ are both equal to zero. We assume that contractile SMCs are initially present only in the media, and at a density of $c_{csmc,0}$ [50]. Random motion is not taken into account for this cell type since contractile SMCs are considered quiescent and do not migrate. Moreover, contractile SMCs are considered unresponsive to growth factors [2].

[Fig. 3 about here.]

(e) Synthetic smooth muscle cells (sSMC)

The synthetic SMCs evolution equation is as follows:

$$\frac{\partial c_{ssmc}}{\partial t} + \underbrace{\nabla \cdot (-D_{ssmc} \nabla c_{ssmc})}_{\text{Random motion}} = \underbrace{k_{diff,csmc} c_{csmc} K_{ssmc,ecm}}_{\substack{\text{Differentiation} \\ \text{from cSMC to sSMC}}} - \\ - \underbrace{k_{diff,ssmc} c_{ssmc} K_{csmc,ecm}}_{\substack{\text{Differentiation} \\ \text{from sSMC to cSMC}}} + \underbrace{k_{prolif,ssmc} \left(c_{gf} - c_{gf,0} \right)}_{\text{Proliferation}} - \underbrace{k_{apop,ssmc} c_{ssmc}}_{\text{Apoptosis}}, \tag{10}$$

where $c_{ssmc}(r, z, t)$ is the synthetic SMCs concentration, D_{ssmc} is the diffusion coefficient of synthetic SMCs in order to simulate the migration process, $k_{prolif,ssmc}$ is the proliferation rate of synthetic SMCs in response to GFs and $k_{apop,ssmc}$ is the apoptosis rate at which synthetic SMCs die. The initial density of synthetic SMCs in the arterial wall, $c_{ssmc,0}$, is assumed to be equal to zero [38].

(f) Endothelial cells:

Along with SMCs, ECs constitute the main cell type within the vasculature. ECs perform a wide variety of significant functions, e.g. cell migration and proliferation, remodelling, apoptosis and the production of different biochemical substances [51], as well as the control of vascular function [52]. Moreover, most of the mechanical responses to flow in the arterial wall, such as shear stress and stretch, directly affect ECs indicating that these cells have specific mechanotransducers capable of transforming mechanical forces into biological responses. A thin single layer of ECs form the endothelium, which in normal conditions, besides being a permeability barrier between the blood flow and the arterial wall, promotes vasodilatation and suppresses intimal hyperplasia by inhibiting inflammation, thrombus formation and SMCs proliferation and migration [53]. However, at sites of injury caused by the stent, the endothelium is denuded [7]. This de-endothelization is considered to be one of the most important mechanisms contributing to restenosis [54]. In this work, it is assumed that the endothelium is denuded between stent struts, considering that only a small amount of cells survive in this region. The behaviour of the ECs may be modeled as:

$$\frac{\partial c_{ec}}{\partial t} + \underbrace{\nabla \cdot (-D_{ec} \nabla c_{ec})}_{\text{Random motion}} = \underbrace{k_{prolif,ec} c_{ec} \left(1 - \frac{c_{ec}}{c_{ec,0}} \right)}_{\text{Proliferation}}, \tag{11}$$

where $c_{ec}(r, z, t)$ is the density of the endothelial cells, D_{ec} is the diffusion coefficient of the ECs to simulate their migration from the lateral edge of the damage blood vessel surface [2] and $k_{prolif,ec}$ is the ECs proliferation rate. ECs can exist only in the intima or subendothelial spaces (SES). The initial concentration of ECs is assumed to be near to zero at sites where the SES is injured and $c_{ec,0}$ [55] at the intact SES. In order to ensure a tractable mathematical model, the equation which governs the behaviour of the ECs is assumed to be independent of the rest of the presented coupled PDEs.

2.4 Tissue growth

We follow the continuum framework for growth of biological tissue developed by Garikipati et al. [56] to describe the tissue growth that leads to restenosis. This formulation considers mass transport and mechanics coupled due to the kinematics of volumetric growth. Accordingly, the balance of mass in the system must satisfy:

$$\frac{\partial \rho_o^i}{\partial t} = \Pi_i - \nabla \cdot \boldsymbol{M}_i, \tag{12}$$

where the index *i* is used to indicate an arbitrary species; ρ_o^i are the concentrations of the species as mass per unit volume in the reference configuration; Π_i are the sources/sinks related to migration, proliferation, differentiation and apoptosis of the cells and synthesis and degradation of the substances and; $\boldsymbol{M}_i$ are the mass fluxes of the *i* arbitrary species. The operators $\nabla(\bullet)$ and $\nabla \cdot (\bullet)$ denote the gradient operator and the divergence of a vector in the reference configuration, respectively. The total material density of the tissue (ρ_o) is the sum of all the individual species concentrations (ρ_o^i), i.e. $\rho_o = \sum_i \rho_o^i$. These concentrations, ρ_o^i, evolve if local volumetric changes take place as a result of mass transport and inter-conversion of species. That implies that the total density in the reference configuration, ρ_o, also changes with time, i.e. as species concentration increases, the material of a species swells, and conversely, shrinks as concentration decreases [56]. Assuming that these volumetric changes are locally isotropic, we can define the following growth deformation gradient tensor, $\boldsymbol{F}_g^i = (\rho_o^i)/(\rho_{orig}^i)\boldsymbol{I}$, where ρ_{orig}^i represents the original concentration of a species in the reference configuration and $\boldsymbol{I}$ is the isotropic tensor of second order. Taking this into consideration, under the small strain hypothesis we can write:

$$\nabla \cdot \boldsymbol{v^i} = \frac{\rho_o^i}{\rho_{orig}^i}, \tag{13}$$

where $\boldsymbol{v}$ is the velocity of the material points [36]. Since the primary components of restenotic tissue are ECs, SMCs and collagen (here represented by ECM), we neglect volume contributions from the other species. Therefore, the isotropic growth that leads restenosis can be finally determined as:

$$\nabla \cdot \boldsymbol{v} = \frac{\partial \Delta c_{ec}}{\partial t} V_{ec} + \frac{\partial \Delta c_{smc}}{\partial t} V_{smc} + \frac{\partial \Delta c_{ecm}}{\partial t} \frac{1}{\rho_{ecm}}, \tag{14}$$

where Δc_{ec} , Δc_{smc} and Δc_{ecm} are the variations of concentrations of ECs, both contractile and synthetic SMCs and ECM, respectively, with respect to the initial concentration of these species before the restenosis process initiation. The parameters V_{ec} and

V_{smc} are the volume of an EC and a SMC, respectively, and ρ_{ecm} is the collagen density (Table 3). To calculate the volume of the individual cells, the shape of the ECs is assumed to be spherical [22] and the SMC shape is assumed to be ellipsoidal or spindle-shaped [57]. Therefore, the volume of each cell type may be estimated as follows:

$$V_{ec} = \frac{4}{3}\pi r_{ec}^3, \tag{15}$$

$$V_{smc} = \frac{4}{3}\pi r_{smc}^2 l_{smc}, \tag{16}$$

where r_{ec} is the typical radius of a EC, r_{smc} and l_{smc} are the typical radius and the length of a SMC, respectively as shown in Table 3. This growth process has been defined following the method described for the development of atherosclerotic plaque in [36] and the fibrosis process after the implantation of an inferior vena cava filter in [38], respectively.

3 Computational model

3.1 Model geometry

A 2D-axisymmetric geometry corresponding to an idealized representation of a straight stented coronary artery segment is considered in all simulations (Fig. 4a). The baseline computational geometry (Table 1) is similar to that introduced by Mongrain et al. [16], also employed by Vairo et al. [18] and modified by Bozsak et al. [19] to study the stent drug release and redistribution in the arterial wall. In order to be able to relate our findings to stent design, we also assess the impact of geometric variations on the final outcome. Specifically, we consider geometrical parameters for three commercial stents, Resolute (Medtronic), Xience (Abbott Vascular) and Biomatrix (Biosensors), whose strut dimensions were obtained from Byrne et al. [58], as well as varying the numbers of struts (n_s), inter-strut spacing (ISS), expansion diameter and level of strut embedment. In total, 9 different geometrical configurations are simulated, as summarised in Table 2.

[Table 1 about here.]

[Table 2 about here.]

[Fig. 4 about here.]

3.2 Boundary conditions

The following boundary conditions were applied to the arterial wall mechanical model: (a) at the lumen-arterial wall interface, $\Gamma_{et,i}$ and $\Gamma_{et,d}$, a constant pressure of 100 mmHg is used to simulate *in vivo* physiological conditions, (b) a displacement of 0.2 mm of the stent struts domain, Ω_s, against the wall is prescribed in order to achieve an extra dilatation of the vessel that is usual in stenting techniques. For the biological species evolution, flux and concentration continuity at the SES-media interface, Γ_{iel}, is prescribed. A zero flux boundary condition, $-\boldsymbol{n} \cdot (-D_j \nabla c_j) = 0$, where $\boldsymbol{n}$ is the unit normal vector to the

corresponding exterior boundary and j denotes each layer of the arterial tissue, was applied at the following boundaries: lumen-wall interface, struts-wall interface, Γ_s, arterial wall inlet, $\Gamma_{j,inlet}$, and outlet, $\Gamma_{j,outlet}$, and outer surface of the media, Γ_{eel}, in case of GFs, MMPs, ECM and SMCs or SES-media interface in case of EC. All computational boundaries and domains are shown in Fig. 4 for the baseline model.

3.3 Numerical methods

The commercial software package COMSOL Multiphysics 5.3 (COMSOL AB, Burlington, MA, USA) was used to create the computational geometry and to solve numerically, by means of the finite element method (FEM), the mechanobiological model detailed in Section 2, which is composed of three coupled systems: (1) a steady system which simulates the mechanical expansion of the stent used for the estimation of the level of damage within the tissue, (2) a transient PDE system which simulates the temporal evolution of the biological species in the arterial wall and, finally, (3) a stationary mechanical analysis to simulate the tissue growth that leads to restenosis. The computational domains (stent struts, intima and media) were meshed using quadratic Lagrange triangular elements, resulting in an overall fine mesh with approximately 150.000 elements (Fig. 4b). A mesh sensitivity analysis was carried out in order to investigate the model mesh independence, testing a series of meshes with different mesh densities. Mesh independence was obtained when there was less than 2% change in the mean concentration of the biological species within the arterial wall for successive mesh refinements. The time-advancing scheme used in the transient problem was a backward differentiation formula (BDF) with variable order of accuracy varying from one to five and variable time stepping. Both stationary and transient problems were solved using a direct linear solver (MUMPS) with relative and absolute tolerance assigned at 10^{-4} and 10^{-3}, respectively.

3.4 Model parameters

Reference values of the parameters included in the governing equations are summarized in Table 3. They correspond to the rates of production, degradation, proliferation and differentiation, the diffusion coefficients of the biological species, the initial concentrations and the threshold values taken into account. Wherever possible, the model input parameters were derived directly from experimental data available in the literature, but in some cases estimation was necessary to ensure that the evolution of the species was broadly consistent with the time-course of restenosis described in some experimental studies [2, 3, 5, 7].

[Table 3 about here.]

3.5 Sensitivity analysis

A sensitivity analysis of the 28 parameters indicated in Table 1 was performed in order to evaluate the effect of varying each input parameter involved on the evolution of the restenosis process and to test the robustness of the results of the computational model. This is of particular importance because of the absence of a complete set of experimental

data and the variability seen in many of the parameters. Computations were carried out for four different values for each parameter apart from the reference value, RV, which is shown in Table 3. The first two values were considered $\pm$ half the reference value of the selected parameter and the other two were given by increasing and decreasing by one order of magnitude, as can be seen in Table 4.

[Table 4 about here.]

4 Results and discussion

The cascade of events occurring within the arterial wall after the stenting procedure and the consequent response of all the biological species are detailed in this section. The level of damage, local concentrations of GFs, MMPs and ECM and local densities of the SMCs and ECs have been evaluated over time at different points of the computational domain, shown in Fig. 5a, in order to show the restenosis evolution and the stability of the model. Points A and C are located close to a central stent strut in the media and in the denuded SES between struts, respectively. Points B and D are situated far away from the stented area in the media and SES, respectively. Moreover, in order to study the evolution of the solute dynamics in the stented domain, where the behaviour of the system will be more affected by the level of damage in the tissue, the distribution of all the species at five different times of the simulation is shown.

4.1 Quantification of damage

The deformed baseline computational geometry is shown in Fig. 5a. The final radii after deployment in the stented and unstented domain were 1.7 mm and 1.5 mm, respectively. Moreover, the total wall thickness was reduced to approximately 0.4 mm in the stented area. Fig. 5b displays the von Mises stress distribution in the arterial wall. The scaling of the stress and the corresponding quantification of the initial damage has been performed is detailed in subsection 3.2.

[Fig. 5 about here.]

4.2 Damage evolution for the baseline model

The local evolution of damage at points A and B is shown in Fig. 6a. At point B, the level of damage is equal to zero at every time, demonstrating that the model does not evolve over time in regions distant from the device. For this reason, local concentrations of substances and local densities of cells at points located far away from the damage caused by the stent remain approximately constant with time. At point A, the level of damage in the tissue decays exponentially with time until the healing process is complete. Fig. 6b shows the distribution of the damage in the stented domain over time. Initially, the highest level of damage is found close to the stent struts and to the regions between the struts, where the endothelium has been denuded. As time proceeds, damage decreases continuously to zero in the radial and longitudinal directions towards the

adventitial boundary and the unstented domain, respectively. The literature suggests that wound healing is variable in duration. Comparing with our results it can be observed that, from day 90, damage is essentially negligible across the entire baseline computational domain, indicating that the healing process is largely complete in agreement with the classical healing response documented in Forrester et al. [2]. This healing process is mainly governed by the evolution of the concentration of MMP as observed in Eq. 3 coupled with the remaining diffusion-reaction equations.

[Fig. 6 about here.]

4.3 Evolution of the species for the baseline model

The results for the GFs evolution are shown in Figs. 7a and 8a. At damaged vascular sites (point A), the local concentration of growth factors initially increases abruptly peaking approximately between 2 to 3 weeks after stent implantation. Following this peak, the concentration decays exponentially over time returning to the physiological baseline value, contributing to the stabilization of the synthetic SMCs, in agreement with the temporal sequence of GFs expression documented in Forrester et al. [2]. As the GFs production depends directly on damage (Eq. 4), at points far from the stented area (point B), the concentration of GFs does not vary over time.

Figs. 7b and 8b show the evolution over time for the MMPs. At the beginning of the simulation the initial concentration of MMP is set to a homeostatic value of $3.83 \cdot 10^{-7}$ $mol \cdot m^{-3}$ [47]. The local concentration of MMP at point A starts increasing, mainly due to its production by the synthetic SMCs, until reaching its maximum value at day 9, which is consistent with the time course of expression of MMP-2 observed by Bendenck et al. [59]. As MMP synthesis depends directly on the level of damage in the tissue, which continues decreasing over time, the effect of the degradation term of Eq. 7 is greater than the effect of the production term and, therefore, the concentration of MMPs starts decreasing until reverting to its normal physiological levels [60].

The collagen variation over time is shown in Figs. 7c and 8c. At early times post-deployment, the local concentration of ECM at point A is degraded as a consequence of the increase of MMPs until reaching a minimum value of 4.02 $mol \cdot m^{-3}$ after 2 days. From this point, its concentration starts increasing over time, mainly because of the differentiation of the contractile SMCs and the proliferation of the synthetic SMCs, producing neointimal thickening in the weeks after injury [7] until an equilibrium value of approximately 7.8 $mol \cdot m^{-3}$ is reached at approximately day 50.

Figs. 7d, 8d and 7e, 8e illustrate the evolution of the contractile and synthetic SMCs, respectively. At the beginning of the process, the local density of the contractile SMCs at point A decreases due to the differentiation into a synthetic phenotype until reaching a minimum value of $2.85 \cdot 10^{13}$ $cell \cdot m^{-3}$ 1-2 weeks after the stenting procedure. Meanwhile, the synthetic SMCs are immediately activated and start proliferating in the media [3]. The local density of synthetic SMCs increases to a value of $3.92 \cdot 10^{12}$ $cell \cdot m^{-3}$ between 2-3 weeks after injury [3], coinciding in time with the peak in the concentration of GFs and demonstrating that locally produced GFs are a major stimulus for SMC migration and proliferation, in agreement with Forrester et al. [2]. After this time, synthetic SMCs begin to revert back to the contractile phenotype. This process continues over several months and is paralleled by a change in the ECM [2]. It can be noted that the evolution

in the concentration of the ECM components, mainly collagen, play a key role in SMCs differentiation, as discussed in subsection 3.3(a), since when the ECM concentration is sufficiently low, synthetic SMCs appear, and when it is sufficiently high, contractile SMCs appear.
Endothelial cells only exist within the intima and their behaviour is governed mainly by proliferation and migration. The time-varying local density profiles of this cell type are shown in Fig. 7f. It can be seen that at points where the endothelium has been denuded by the stent (i.e. point C), ECs start proliferating at the beginning of the restenotic process. Between days 100 to 150 they cease proliferation, reaching, at approximately day 180, an equilibrium density of $5{\cdot}10^{11}$ cell$\cdot$m^{-3} [55] along the length of the SES, corresponding to homeostatic conditions and in agreement with the temporal response described by Forrester et al. [2]. It can be considered then that the endothelium has been completely restored. However, after this time restenotic events continue since both SMCs proliferation/migration and ECM deposition does not necessarily cease at this time.

[Fig. 7 about here.]

[Fig. 8 about here.]

4.4 Sensitivity analysis

The results for the sensitivity analysis performed involving those parameters that have shown to have a greater influence on the behaviour of the system are shown in Figs. 9 and 10. The discussion is included in the online Supplementary Material.

[Fig. 9 about here.]

[Fig. 10 about here.]

4.5 Tissue growth

The volumetric growth of new tissue into the lumen of the vessel in response to the mechanical injury caused by the medical device after 300 days is shown in Fig. 11, for the baseline model. It should be noticed that the restenotic tissue grows considerably between struts. The degree of occlusion can be measured in terms of the diameter or area of restenosis [61]. In this work, the change in the cross-sectional area of the model is used as a measure of measuring arterial restenosis. The percentage of stenosis is calculated as $(1 - A_r/A_{ref}) \cdot 100$, where A_r and A_{ref} are the area of the lesion and of the reference site, respectively. Therefore, the resulting degree of restenosis after 300 days is approximately 25% for the baseline set of parameters simulated in broad agreement with the clinical data presented in Nobuyoshi et al. [62].

[Fig. 11 about here.]

4.6 Impact of geometric variations on tissue growth

In Figure 12, we consider the impact of different geometric configurations on the % restenosis for the various cases considered in Table 2. The model produces different levels of restenosis depending on the geometric parameters, and our results are in qualitative agreement with clinical observations. Specifically, the results of our simulations show that % restenosis:

- increases with increasing strut diameter;
- decreases with an increase in inter-strut spacing;
- increases with an increase in lumen expansion diameter;
- depends on the strut embedment configuration.

[Fig. 12 about here.]

5 Limitations

We would like to emphasize that there are a number of limitations in this work, as we now discuss.

5.1 Validation

Whilst the continuum approach that we have adopted is advantageous in that it allows us to assess how the evolution of the various species affects the overall healing process, the disadvantage is that it is extremely difficult to measure spatiotemporal cellular densities and growth factor concentrations experimentally. Certainly, we are not aware of how such validation may be obtained *in vivo*. In short, we do not believe that the data currently exists to validate the predictions of the model at the level of individual concentrations/densities in space and in time. Therein lies the major advantage of the continuum model proposed here, i.e. the ability to simulate the evolution of species which we cannot get insight into from *in vivo* experiments. Notwithstanding, we have compared our results to restenosis data (at the tissue level) and have shown that our model is in broad agreement with what is seen in the clinic.

5.2 Flow modelling

We acknowledge that there is a known link between the level of shear stress and restenosis. Indeed, most haemodynamics models that assess different stent designs and patient-specific geometries set out to predict quantities such as wall shear stress (WSS), oscillatory shear index (OSI) and time averaged wall shear stress (TAWSS), because these can be related to clinical outcome. Keller et al. [63], for example, investigated the correlation between mechanical and fluid stresses and the magnitude of restenosis, and found that whilst a linear correlation is not obtained when these stimuli are considered separately, there is a closer correlation when the combined action of these stimuli is considered. Whilst such correlations are useful for providing insight into the influence of force on restenosis, what is less clear, is precisely *how* the transmission of fluid forces affects

the behaviour of the cells and other species involved in the healing response. The most sophisticated model of restenosis to date (Zun et al. [29]) does include the effects of flow, but in in an indirect way. Specifically, Zun et al. assume that neointimal growth is dictated by nitric oxide (NO) production, which is governed by average WSS. Therefore, Zun et al. calculate WSS from a steady laminar flow simulation and pass this to their biological solver, where the level of NO dictates the ensuing biological response through a set of rules. In the absence of data resolving the underlying physics of how the transmission of force generated by flow affects the healing process *in vivo*, the influence of flow has been neglected in the present analysis. Certainly, the force generated by flow would influence the parameters of our model: in this sense, the sensitivity analysis could be seen to indirectly incorporate the effects of varying flow.

5.3 Geometry

Concerning the geometry of the FE model, a 2D axisymmetric geometry corresponding to an idealized representation of a straight segment of a healthy coronary artery has been considered in this study. This could be improved using more realistic geometries of the artery, such us coronary arteries with curvature, bifurcations, presence of atherosclerotic plaque or derived directly from 3D patient-specific geometries. However, such models would considerably increase the cost of the numerical simulations and are left for future work.

5.4 Damage modelling

In this work, following the approach presented by Zahedmanesh et al. [22], the modelling of the initial damage in the tissue after stenting is considered in a very simple way, which is based on the ultimate tensile stress-stretch response for each layer of human coronary arteries [42]. However, to our knowledge, there is no experimental data published in the literature which directly relates the levels of stress-strain due to stent deployment to the arterial wall injury and the sequence of events associated such as GFs and MMPs production, synthesis, number of proliferating SMCs, etc.

5.5 Model parameters and biological species

The biological parameters involved in this model were obtained from a wide range of *in vivo* and *in vitro* experiments from the published literature on different blood vessels from human and animal models. However, due to the important structural and functional differences between arteries [48], these parameters could vary from artery-to-artery, species-to-species and patient-to-patient, or even from one lesion to another in the same patient. Additionally, some of these parameters have had to be estimated to be consistent with the time course of the restenosis process found in different studies [2–5, 7]. Moreover, all the parameters have been taken as constant and uniform through the whole artery, but in fact they are very likely to change produced during the process. Finally, only the most important biological species have been taken into account. Other species involved in the coronary restenosis process such as platelets, monocytes, different classes of GFs (PDGF, EGF, IGF, TGF, FGF), mesenchymal cells, fibroblasts,

collagen subtypes, proteoglycans, fibronectin, etc. have been grouped or omitted. Moreover, only the main biological processes have been considered in this model. Other processes such as activation and migration of the mesenchymal stem cells, release of GFs by fibroblasts or ECM synthesis by ECs were not included.

6 Conclusions

A mathematical and computational model which successfully captures the main characteristics of the restenosis process after stent implantation in a healthy coronary artery has been presented in this work. A continuum approach has been taken into account for modelling the behaviour of the different biological species involved in ISR, resulting in a PDE system of several coupled diffusion-reaction equations, solved numerically by means of FEM. Mechanical damage, which is quantitatively estimated as a function of the von Mises stress levels obtained in the arterial wall after a FE simulation of the stent expansion, is considered as the stimulus needed to start the process.

Our results confirm that ISR depends on multiple factors, with the ECM dynamics and SMCs proliferation the primary contributors to its pathogenesis. In addition to this, the sensitivity analysis carried out for the different model parameters, as well as providing information on the stability of the model, provides us with an understanding of how changes in one parameter will affect the behaviour of the whole system. The value of $k_{deg,d}$ has a significant impact on the healing rate. Moreover, it was shown that the rates of production, degradation, differentiation and proliferation taken into account highly affect the local levels of concentration/density of the species involved in the process and the temporal response of the system. The apoptosis rate of synthetic SMCs, diffusion coefficients and initial conditions also influence the evolution of the model, although to a lesser extent.

In conclusion, in spite of the simplifications and limitations we have discussed, the model developed is able to capture some of the underlying mechanisms and patterns of ISR. Moreover, the results obtained are in good agreement with clinical hypotheses relating to ISR occurrence. Therefore, this model can be considered as a step forward to a better understanding of this phenomenon.

7 Author Contributions

Conceived and designed the study: MM, SM, EP. Development of Mathematical Model: JE, MM, SM, EP. Computational Implementation of model: JE. Writing, review and editing: JE, MM, SM, EP.

8 Acknowledgements and funding statement

The authors gratefully acknowledge funding provided by the Spanish Ministry of Economy, Industry and Competitiveness under research project number DPI2016-76630-C2-1-R and grant number BES-2014-069737.

9 Data Accessibility

The data associated with this paper consists of the mathematical models and their numerical solution as detailed in the text.

References

1. Wilkins E, Wilson L, Wickramasinghe K, Bhatnagar P, Leal J, Luengo-Fernandez R, et al. European cardiovascular disease statistics 2017. European Heart Network, Brussels. 2017;p. 192.
2. Forrester JS, Fishbein M, Helfant R, Fagin J. A paradigm for restenosis based on cell biology: clues for the development of new preventive therapies. Journal of the American College of Cardiology. 1991;17(3):758–769.
3. Bauters C, Isner JM. The biology of restenosis. Progress in Cardiovascular Diseases. 1997;40(2):107–116.
4. Libby P, Tanaka H. The molecular bases of restenosis. Progress in cardiovascular diseases. 1997;40(2):97–106.
5. Welt FG, Rogers C. Inflammation and restenosis in the stent era. Arteriosclerosis, Thrombosis, and Vascular Biology. 2002;22(11):1769–1776.
6. Bennett MR. In-stent stenosis: pathology and implications for the development of drug eluting stents. Heart. 2003;89(2):218–224.
7. Costa MA, Simon DI. Molecular basis of restenosis and drug-eluting stents. Circulation. 2005;111(17):2257–2273.
8. Buccheri D, Piraino D, Andolina G, Cortese B. Understanding and managing in-stent restenosis: a review of clinical data, from pathogenesis to treatment. Journal of Thoracic Disease. 2016;8(10):E1150.
9. Schwartz RS, Huber KC, Murphy JG, Edwards WD, Camrud AR, Vlietstra RE, et al. Restenosis and the proportional neointimal response to coronary artery injury: results in a porcine model. Journal of the American College of Cardiology. 1992;20(5):1284–1293.
10. Kornowski R, Hong MK, Tio FO, Bramwell O, Wu H, Leon MB. In-stent restenosis: contributions of inflammatory responses and arterial injury to neointimal hyperplasia. Journal of the American College of Cardiology. 1998;31(1):224–230.
11. McHugh P, Barakat A, McGinty S. Medical stents: state of the art and future directions. Annals of Biomedical Engineering. 2016;44(2):274–275.
12. Migliavacca F, Petrini L, Massarotti P, Schievano S, Auricchio F, Dubini G. Stainless and shape memory alloy coronary stents: a computational study on the interaction with the vascular wall. Biomechanics and Modeling in Mechanobiology. 2004;2(4):205–217.
13. Zahedmanesh H, Kelly DJ, Lally C. Simulation of a balloon expandable stent in a realistic coronary artery: Determination of the optimum modelling strategy. Journal of Biomechanics. 2010;43(11):2126–2132.
14. García A, Peña E, Martínez M. Influence of geometrical parameters on radial force during self-expanding stent deployment. Application for a variable radial stiffness stent. Journal of the Mechanical Behavior of Biomedical Materials. 2012;10:166–175.
15. Conway C, McGarry J, McHugh P. Modelling of atherosclerotic plaque for use in a computational test-bed for stent angioplasty. Annals of Biomedical Engineering. 2014;42(12):2425–2439.
16. Mongrain R, Leask R, Brunette J, Faik I, Bulman-Feleming N, Nguyen T. Numerical modeling of coronary drug eluting stents. Studies in Health Technology and Informatics. 2005;113:443–458.
17. Migliavacca F, Gervaso F, Prosi M, Zunino P, Minisini S, Formaggia L, et al. Expansion and drug elution model of a coronary stent. Computer Methods in Biomechanics and Biomedical Engineering. 2007;10(1):63–73.
18. Vairo G, Cioffi M, Cottone R, Dubini G, Migliavacca F. Drug release from coronary eluting stents: a multidomain approach. Journal of biomechanics. 2010;43(8):1580–1589.
19. Bozsak F, Chomaz JM, Barakat AI. Modeling the transport of drugs eluted from stents: physical phenomena driving drug distribution in the arterial wall. Biomechanics and Modeling in Mechanobiology. 2014;13(2):327–347.
20. McGinty S, Pontrelli G. On the role of specific drug binding in modelling arterial eluting stents. Journal of Mathematical Chemistry. 2016;54(4):967–976.
21. Zahedmanesh H, Lally C. A multiscale mechanobiological modelling framework using agent-based models and finite element analysis: application to vascular tissue engineering. Biomechanics and Modeling in Mechanobiology. 2012;11(3):363–377.

22. Zahedmanesh H, Van Oosterwyck H, Lally C. A multi-scale mechanobiological model of in-stent restenosis: deciphering the role of matrix metalloproteinase and extracellular matrix changes. Computer Methods in Biomechanics and Biomedical Engineering. 2014;17(8):813–828.
23. Boyle C, Lennon AB, Early M, Kelly D, Lally C, Prendergast P. Computational simulation methodologies for mechanobiological modelling: a cell-centred approach to neointima development in stents. Philosophical Transactions of the Royal Society of London A: Mathematical, Physical and Engineering Sciences. 2010;368(1921):2919–2935.
24. Boyle CJ, Lennon AB, Prendergast PJ. In silico prediction of the mechanobiological response of arterial tissue: application to angioplasty and stenting. Journal of Biomechanical Engineering. 2011;133(8):081001.
25. Boyle CJ, Lennon AB, Prendergast PJ. Application of a mechanobiological simulation technique to stents used clinically. Journal of Biomechanics. 2013;46(5):918–924.
26. Keshavarzian M, Meyer CA, Hayenga HN. Mechanobiological model of arterial growth and remodeling. Biomechanics and Modeling in Mechanobiology. 2017;p. 1–15.
27. Evans DJ, Lawford PV, Gunn J, Walker D, Hose D, Smallwood R, et al. The application of multiscale modelling to the process of development and prevention of stenosis in a stented coronary artery. Philosophical Transactions of the Royal Society of London A: Mathematical, Physical and Engineering Sciences. 2008;366(1879):3343–3360.
28. Tahir H, Niculescu I, Bona-Casas C, Merks R, Hoekstra A. An in silico study on the role of smooth muscle cell migration in neointimal formation after coronary stenting. Journal of the Royal Society Interface. 2015;12:20150358.
29. Zun P, Anikina T, Svitenkov A, Hoekstra A. A Comparison of Fully-Coupled 3D In-Stent Restenosis Simulations to In-vivo Data. Frontiers in Physiology. 2017;8:284.
30. Rachev A, Manoach E, Berry J, Moore Jr J. A model of stress-induced geometrical remodeling of vessel segments adjacent to stents and artery/graft anastomoses. Journal of Theoretical Biology. 2000;206(3):429–443.
31. Hoffmann R, Mintz GS, Dussaillant GR, Popma JJ, Pichard AD, Satler LF, et al. Patterns and mechanisms of in-stent restenosis: a serial intravascular ultrasound study. Circulation. 1996;94(6):1247–1254.
32. Budu-Grajdeanu P, Schugart RC, Friedman A, Valentine C, Agarwal AK, Rovin BH. A mathematical model of venous neointimal hyperplasia formation. Theoretical Biology and Medical Modelling. 2008;5(1):2.
33. Calvez V, Ebde A, Meunier N, Raoult A. Mathematical modelling of the atherosclerotic plaque formation. In: ESAIM: Proceedings. vol. 28. EDP Sciences; 2009. p. 1–12.
34. Ibragimov A, Ritter L, Walton JR. Stability analysis of a reaction-diffusion system modeling atherogenesis. SIAM Journal on Applied Mathematics. 2010;70(7):2150–2185.
35. El Khatib N, Génieys S, Kazmierczak B, Volpert V. Reaction–diffusion model of atherosclerosis development. Journal of Mathematical Biology. 2012;65(2):349–374.
36. Cilla M, Peña E, Martínez MA. Mathematical modelling of atheroma plaque formation and development in coronary arteries. Journal of The Royal Society Interface. 2014;11(90):20130866.
37. Su J, Gonzales HP, Todorov M, Kojouharov H, Tang L. A mathematical model for foreign body reactions in 2D. International journal of computer mathematics. 2011;88(3):610–633.
38. Nicolás M, Peña E, Malvè M, Martínez M. Mathematical modeling of the fibrosis process in the implantation of inferior vena cava filters. Journal of Theoretical Biology. 2015;387:228–240.
39. Fereidoonnezhad B, Naghdabadi R, Sohrabpour S, Holzapfel G. A mechanobiological model for damage-induced growth in arterial tissue with application to in-stent restenosis. Journal of the Mechanics and Physics of Solids. 2017;101:311–327.
40. Marino M, Pontrelli G, Vairo G, Wriggers P. A chemo-mechano-biological formulation for the effects of biochemical alterations on arterial mechanics: the role of molecular transport and multiscale tissue remodelling. Journal of The Royal Society Interface. 2017;14(136):20170615.
41. Yeoh OH. Some forms of the strain energy function for rubber. Rubber Chemistry and technology. 1993;66(5):754–771.
42. Holzapfel GA, Sommer G, Gasser CT, Regitnig P. Determination of layer-specific mechanical properties of human coronary arteries with nonatherosclerotic intimal thickening and related constitutive modeling. American Journal of Physiology-Heart and Circulatory Physiology. 2005;289(5):H2048–H2058.
43. Jukema JW, Verschuren JJ, Ahmed TA, Quax PH. Restenosis after PCI. Part 1: pathophysiology and risk factors. Nature Reviews Cardiology. 2012;9(1):53.
44. McLaren J, Prentice A, Charnock-Jones D, Smith S. Vascular endothelial growth factor (VEGF) concentrations are elevated in peritoneal fluid of women with endometriosis. Human Reproduction. 1996;11(1):220–223.

45. Matrisian LM. The matrix-degrading metalloproteinases. Bioessays. 1992;14(7):455–463.
46. Newby AC. Matrix metalloproteinases regulate migration, proliferation, and death of vascular smooth muscle cells by degrading matrix and non-matrix substrates. Cardiovascular Research. 2006;69(3):614–624.
47. Sáez P, Peña E, Martínez MÁ, Kuhl E. Mathematical modeling of collagen turnover in biological tissue. Journal of Mathematical Biology. 2013;67(6-7):1765–1793.
48. Robertson AM, Watton PN. Mechanobiology of the arterial wall. Modeling of transport in biological media Elsevier, New York. 2013;p. 275–347.
49. Thyberg J, Blomgren K, Roy J, Tran PK, Hedin U. Phenotypic modulation of smooth muscle cells after arterial injury is associated with changes in the distribution of laminin and fibronectin. Journal of Histochemistry & Cytochemistry. 1997;45(6):837–846.
50. Tracy RE. Declining density of intimal smooth muscle cells as a precondition for atheronecrosis in the coronary artery. Virchows Archiv: European Journal of Pathology. 1997;430(2):155–162.
51. Chien S. Mechanotransduction and endothelial cell homeostasis: the wisdom of the cell. American Journal of Physiology-Heart and Circulatory Physiology. 2007;292(3):H1209–H1224.
52. Michiels C. Endothelial cell functions. Journal of cellular physiology. 2003;196(3):430–443.
53. Marx SO, Totary-Jain H, Marks AR. Vascular smooth muscle cell proliferation in restenosis. Circulation: Cardiovascular Interventions. 2011;4(1):104–111.
54. Kipshidze N, Dangas G, Tsapenko M, Moses J, Leon MB, Kutryk M, et al. Role of the endothelium in modulating neointimal formation: vasculoprotective approaches to attenuate restenosis after percutaneous coronary interventions. Journal of the American College of Cardiology. 2004;44(4):733–739.
55. Farcas MA, Rouleau L, Fraser R, Leask RL. The development of 3-D, in vitro, endothelial culture models for the study of coronary artery disease. Biomedical Engineering Online. 2009;8(1):30.
56. Garikipati K, Arruda E, Grosh K, Narayanan H, Calve S. A continuum treatment of growth in biological tissue: the coupling of mass transport and mechanics. Journal of the Mechanics and Physics of Solids. 2004;52(7):1595–1625.
57. Martini F, Nath J, EF B. Fundamentals of anatomy & physiology. Science P, editor. Pearson; 2014.
58. Byrne RA, Joner M, Kastrati A. Stent thrombosis and restenosis: what have we learned and where are we going? The Andreas Grüntzig Lecture ESC 2014. European Heart Journal. 2015;36(47):3320–3331.
59. Bendeck MP, Zempo N, Clowes AW, Galardy RE, Reidy MA. Smooth muscle cell migration and matrix metalloproteinase expression after arterial injury in the rat. Circulation Research. 1994;75(3):539–545.
60. George SJ, Zaltsman AB, Newby AC. Surgical preparative injury and neointima formation increase MMP-9 expression and MMP-2 activation in human saphenous vein. Cardiovascular Research. 1997;33(2):447–459.
61. Ota H, Takase K, Rikimaru H, Tsuboi M, Yamada T, Sato A, et al. Quantitative vascular measurements in arterial occlusive disease. Radiographics. 2005;25(5):1141–1158.
62. Nobuyoshi M, Kimura T, Nosaka H, Mioka S, Ueno K, Yokoi H, et al. Restenosis after successful percutaneous transluminal coronary angioplasty: serial angiographic follow-up of 229 patients. Journal of the American College of Cardiology. 1988;12(3):616–623.
63. Keller BK, Amatruda CM, Hose DR, Gunn J, Lawford PV, Dubini G, et al. Contribution of mechanical and fluid stresses to the magnitude of in-stent restenosis at the level of individual stent struts. Cardiovascular Engineering and Technology. 2014;5(2):164–175.
64. Dodge Jr JT, Brown BG, Bolson EL, Dodge HT. Lumen diameter of normal human coronary arteries. Influence of age, sex, anatomic variation, and left ventricular hypertrophy or dilation. Circulation. 1992;86(1):232–246.
65. Sherratt J, Murray J. Mathematical analysis of a basic model for epidermal wound healing. Journal of Mathematical Biology. 1991;29(5):389–404.
66. Rossi F, Casalini T, Raffa E, Masi M, Perale G. Bioresorbable polymer coated drug eluting stent: a model study. Molecular Pharmaceutics. 2012;9(7):1898–1910.
67. Schwartz RS, Chu A, Edwards WD, Srivatsa SS, Simari RD, Isner JM, et al. A proliferation analysis of arterial neointimal hyperplasia: lessons for antiproliferative restenosis therapies. International journal of cardiology. 1996;53(1):71–80.
68. Sagi I, Gaffney J. Matrix metalloproteinase biology. Sagi I, Gaffney J, editors. John Wiley & Sons; 2015.
69. Lally C, Prendergast P. Simulation of in-stent restenosis for the design of cardiovascular stents. In: Mechanics of Biological Tissue. Springer; 2006. p. 255–267.

Parameter	Description	Value	Reference
r_l	Lumen initial radius	1.2 mm	[64]
δ_{ses}	Intima thickness	0.01 mm	[19]
δ_m	Media thickness	0.5 mm	[17]
r_s	Strut radius	0.125 mm	[16]
w_s	Interstrut distance	0.7 mm	[16]

Table 1: List of parameters related to the geometry of the baseline model.

Case	Stent model	Strut shape	Strut size (μm)	ISS (mm)	n_s	Emb. config.	Ratio
0	Baseline model	circular	250	0.7	10	50%	1.1
1	Resolute (Medtronic)	circular	91	0.7	10	50%	1.1
2	Xience (Abbott)	square	81	0.7	10	50%	1.1
3	Biomatrix (Biosensors)	square	120	0.7	10	50%	1.1
4	Baseline model	circular	250	1.4	5	50%	1.1
5	Baseline model	circular	250	1.0	7	50%	1.1
6	Baseline model	circular	250	0.5	14	50%	1.1
7	Baseline model	circular	250	0.7	10	25-75%	1.1
8	Baseline model	circular	250	0.7	10	50%	1.2

Table 2: List of cases simulated to relate our findings to stent design. The last colum refers to the ratio of the lumen diameter after stent expansion to the lumen diameter before stent expansion.

Parameter	Description	Value	Reference
	Rates		
$k_{deg,d}$	Damage degradation	0.5 $m^3 \cdot mol^{-1} \cdot s^{-1}$	Estimated
$k_{prod,gf}$	GF production	$8 \cdot 10^{-13}$ $mol \cdot m^{-3} \cdot s^{-1}$	Estimated
$k_{deg,gf}$	GF degradation	$1.27 \cdot 10^{-6}$ s^{-1}	[24]- [65]
$k_{prod1,mmp}$	MMP production by cSMC	$3 \cdot 10^{-26}$ $mol \cdot cell^{-1} \cdot s^{-1}$	Adapted from [22]
$k_{prod2,mmp}$	MMP production by sSMC	$6 \cdot 10^{-26}$ $mol \cdot cell^{-1} \cdot s^{-1}$	Adapted from [22]
$k_{deg,mmp}$	MMP degradation	$4.63 \cdot 10^{-6}$ s^{-1}	[24]
$k_{prod,ecm}$	ECM production by sSMC	$2.157 \cdot 10^{-11}$ $g \cdot cell^{-1} \cdot s^{-1}$	[36]
$k_{deg,ecm}$	ECM degradation	$2 \cdot 10^{3}$ s^{-1}	Estimated
$k_{diff,csmc}$	cSMC differentiation	$5 \cdot 10^{-7}$ s^{-1}	[23]- [36]
$k_{diff,ssmc}$	sSMC differentiation	$2.314 \cdot 10^{-6}$ s^{-1}	[23]
$k_{prolif,ssmc}$	sSMC proliferation by GF	$2.5 \cdot 10^{13}$ $cell \cdot mol^{-1} \cdot s^{-1}$	Estimated
$k_{apop,ssmc}$	sSMC apoptosis	$2.2 \cdot 10^{-10}$ s^{-1}	[66]
$k_{prolif,ec}$	EC proliferation	10^{-6} s^{-1}	Adapted from [67]
	Diffusion coefficients		
D_{gf}	Growth Factors	$2.6 \cdot 10^{-11}$ $m^2 \cdot s^{-1}$	[32]
D_{mmp}	Matrix Metalloproteinases	$1.2 \cdot 10^{-12}$ $m^2 \cdot s^{-1}$	[68]
D_{ecm}	Extracellular Matrix	Neglected	[36]
D_{csmc}	Contractile Smooth Muscle Cells	Neglected	[36]
D_{ssmc}	Synthetic Smooth Muscle Cells	$1.85 \cdot 10^{-13}$ $m^2 \cdot s^{-1}$	[69]
D_{ec}	Endothelial Cells	$8 \cdot 10^{-14}$ $m^2 \cdot s^{-1}$	[32]
	Initial concentrations		
$c_{gf,0}$	GF initial concentration	$3.48 \cdot 10^{-7}$ $mol \cdot m^{-3}$	[44]
$c_{mmp,0}$	MMP initial concentration	$3.83 \cdot 10^{-7}$ $mol \cdot m^{-3}$	[47]
$c_{ecm,0}$	ECM initial concentration	6.67 $mol \cdot m^{-3}$	[47]
$c_{csmc,0}$	cSMC initial concentration	$3.16 \cdot 10^{13}$ $cell \cdot m^{-3}$	[50]
$c_{ssmc,0}$	sSMC initial concentration	0 $cell \cdot m^{-3}$	[38]
$c_{ec,0}$	EC initial concentration	$5 \cdot 10^{11}$ $cell \cdot m^{-3}$	[55]
	Threshold values		
$c_{gf,th}$	GF threshold concentration	$10 \cdot c_{gf,0}$	Estimated
$c_{mmp,th}$	MMP threshold concentration	$10 \cdot c_{mmp,0}$	Estimated
$c_{ecm,th}$	ECM threshold	$c_{ecm,0}$	[38]
$c_{ecm,th1}$	ECM superior threshold	$1.5 \cdot c_{ecm,0}$	Estimated
$c_{ecm,th2}$	ECM inferior threshold	$0.1 \cdot c_{ecm,0}$	Estimated
	Growth model		
r_{ec}	Endothelial cell radius	17.87 μm	[22]
r_{smc}	SMC radius	3.75 μm	[57]
l_{smc}	SMC length	115 μm	[57]
ρ_{ecm}	ECM density	1 $g \cdot ml^{-1}$	[47]

Table 3: List of parameters related to the biological model.

Case	Parameter	Unit	RV/10	RV/2	RV	2RV	10 RV
01	$k_{deg,d}$	$m^3 \cdot mol^{-1} \cdot s^{-1}$	0.05	0.25	0.5	1	5
02	$k_{prod,gf}$	$mol \cdot m^{-3} \cdot s^{-1}$	$8 \cdot 10^{-14}$	$4 \cdot 10^{-13}$	$8 \cdot 10^{-13}$	$1.6 \cdot 10^{-12}$	$8 \cdot 10^{-12}$
03	$k_{deg,gf}$	s^{-1}	$1.27 \cdot 10^{-7}$	$6.35 \cdot 10^{-7}$	$1.27 \cdot 10^{-6}$	$2.54 \cdot 10^{-6}$	$1.27 \cdot 10^{-5}$
04	$k_{prod1,mmp}$	$mol \cdot cell^{-1} \cdot s^{-1}$	$3 \cdot 10^{-27}$	$1.5 \cdot 10^{-26}$	$3 \cdot 10^{-26}$	$6 \cdot 10^{-26}$	$3 \cdot 10^{-25}$
05	$k_{prod2,mmp}$	$mol \cdot cell^{-1} \cdot s^{-1}$	$6 \cdot 10^{-27}$	$3 \cdot 10^{-26}$	$6 \cdot 10^{-26}$	$1.2 \cdot 10^{-25}$	$6 \cdot 10^{-25}$
06	$k_{deg,mmp}$	s^{-1}	$4.63 \cdot 10^{-7}$	$2.31 \cdot 10^{-6}$	$4.63 \cdot 10^{-6}$	$9.26 \cdot 10^{-6}$	$4.63 \cdot 10^{-5}$
07	$k_{prod,ecm}$	$g \cdot cell^{-1} \cdot s^{-1}$	$2.15 \cdot 10^{-12}$	$1.07 \cdot 10^{-11}$	$2.15 \cdot 10^{-11}$	$4.31 \cdot 10^{-11}$	$2.15 \cdot 10^{-10}$
08	$k_{deg,ecm}$	s^{-1}	$2 \cdot 10^{2}$	$1 \cdot 10^{3}$	$2 \cdot 10^{3}$	$4 \cdot 10^{3}$	$2 \cdot 10^{4}$
09	$k_{diff,csmc}$	s^{-1}	$5 \cdot 10^{-8}$	$2.5 \cdot 10^{-7}$	$5 \cdot 10^{-7}$	$\cdot 10^{-6}$	$5 \cdot 10^{-6}$
10	$k_{diff,ssmc}$	s^{-1}	$2.31 \cdot 10^{-7}$	$1.15 \cdot 10^{-6}$	$2.31 \cdot 10^{-6}$	$4.62 \cdot 10^{-6}$	$2.31 \cdot 10^{-5}$
11	$k_{prolif,ssmc}$	$cell \cdot mol^{-1} \cdot s^{-1}$	$2.5 \cdot 10^{12}$	$1.25 \cdot 10^{13}$	$2.5 \cdot 10^{13}$	$5 \cdot 10^{13}$	$2.5 \cdot 10^{14}$
12	$k_{apop,ssmc}$	s^{-1}	$2.2 \cdot 10^{-11}$	$1.1 \cdot 10^{-10}$	$2.2 \cdot 10^{-10}$	$4.4 \cdot 10^{-10}$	$2.2 \cdot 10^{-9}$
13	$k_{prolif,ec}$	s^{-1}	10^{-7}	$5 \cdot 10^{-7}$	10^{-6}	$2 \cdot 10^{-6}$	10^{-5}
14	D_{gf}	$m^2 \cdot s^{-1}$	$2.6 \cdot 10^{-12}$	$1.3 \cdot 10^{-11}$	$2.6 \cdot 10^{-11}$	$5.2 \cdot 10^{-11}$	$2.6 \cdot 10^{-10}$
15	D_{mmp}	$m^2 \cdot s^{-1}$	$1.2 \cdot 10^{-13}$	$6 \cdot 10^{-13}$	$1.2 \cdot 10^{-12}$	$2.4 \cdot 10^{-12}$	$1.2 \cdot 10^{-11}$
16	D_{ssmc}	$m^2 \cdot s^{-1}$	$1.85 \cdot 10^{-14}$	$9.26 \cdot 10^{-13}$	$1.85 \cdot 10^{-13}$	$3.7 \cdot 10^{-13}$	$1.85 \cdot 10^{-12}$
17	D_{ec}	$m^2 \cdot s^{-1}$	$8 \cdot 10^{-15}$	$4 \cdot 10^{-14}$	$8 \cdot 10^{-14}$	$1.6 \cdot 10^{-13}$	$8 \cdot 10^{-13}$
18	$c_{gf,0}$	$mol \cdot m^{-3}$	$3.48 \cdot 10^{-8}$	$1.74 \cdot 10^{-7}$	$3.48 \cdot 10^{-7}$	$6.96 \cdot 10^{-7}$	$3.48 \cdot 10^{-6}$
19	$c_{mmp,0}$	$mol \cdot m^{-3}$	$3.83 \cdot 10^{-8}$	$1.91 \cdot 10^{-7}$	$3.83 \cdot 10^{-7}$	$7.66 \cdot 10^{-7}$	$3.83 \cdot 10^{-6}$
20	$c_{ecm,0}$	$mol \cdot m^{-3}$	0.667	3.335	6.67	13.33	66.7
21	$c_{csmc,0}$	$cell \cdot m^{-3}$	$3.16 \cdot 10^{12}$	$1.58 \cdot 10^{13}$	$3.16 \cdot 10^{13}$	$6.32 \cdot 10^{13}$	$3.16 \cdot 10^{14}$
22*	$c_{ssmc,0}$	$cell \cdot m^{-3}$	0 (RV)	$3.16 \cdot 10^{12}$	$1.58 \cdot 10^{13}$	$3.16 \cdot 10^{13}$	-
23	$c_{ec,0}$	$cell \cdot m^{-3}$	$5 \cdot 10^{10}$	$2.5 \cdot 10^{11}$	$5 \cdot 10^{11}$	$1 \cdot 10^{12}$	$5 \cdot 10^{12}$
24	$c_{gf,th}$	$mol \cdot m^{-3}$	$3.48 \cdot 10^{-7}$	$1.74 \cdot 10^{-6}$	$3.48 \cdot 10^{-6}$	$6.96 \cdot 10^{-6}$	$3.48 \cdot 10^{-5}$
25	$c_{mmp,th}$	$mol \cdot m^{-3}$	$3.83 \cdot 10^{-7}$	$1.91 \cdot 10^{-6}$	$3.83 \cdot 10^{-6}$	$7.66 \cdot 10^{-6}$	$3.83 \cdot 10^{-5}$
26	$c_{ecm,th}$	$mol \cdot m^{-3}$	0.667	3.335	6.67	13.33	66.7
27	$c_{ecm,th1}$	$mol \cdot m^{-3}$	1	5	10	20	100
28	$c_{ecm,th2}$	$mol \cdot m^{-3}$	0.067	0.333	0.667	1.333	6.67

Table 4: List of cases with the corresponding parameter values computed in the sensitivity analysis. (*) Note that due to the reference value of $c_{ssmc,0}$ in case 22, being equal to zero, the strategy for varying parameters had to be adjusted. Points A and C are located close to a central stent strut in the media and in the denuded SES between struts, respectively. Points B and D are situated far away from the stented area in the media and SES, respectively.

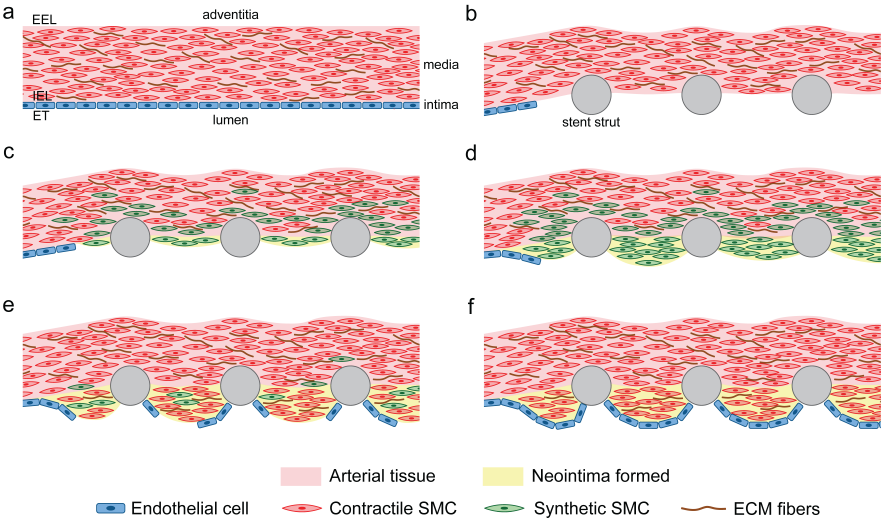

Fig. 1: Schematic representation of ISR. In summary, prior to stent deployment, SMCs exist in a quiescent and contractile phenotype predominantly in the media layer of the tissue and ECs populate the uninjured arterial wall (a). After stent deployment (b), endothelial denudation, atherosclerotic plaque compression (often with dissection into the media and occasionally adventitia), and unphysiological stretch of the entire artery occur [7]. Platelets are then deposited at the injured area and GFs are released. Local increases in stationary mechanical strain, which occurs following stenting, lead to up-regulation of MMP by SMCs and degradation of collagen in the ECM. Endothelial damage and denudation, among multiple factors, lead to the phenotype switch of medial SMCs from a contractile to a synthetic state [3]. Synthetic SMCs proliferate in response to GFs [24] first in the media and then these begin to migrate towards the injured area (c, d). Simultaneously, ECs migrate from the lateral edge of the damaged blood vessel surface [2] (e). Moreover, synthetic SMCs secrete ECM components, such as collagen and proteoglycans, which constitute the neointimal lesion [24]. Between 2-3 weeks after the stenting procedure, synthetic SMCs begin to revert to the contractile phenotype [2]. Neointima typically increases up to three months after the procedure, with little change to six months and a gradual reduction between six months to three years [6] (e, f).

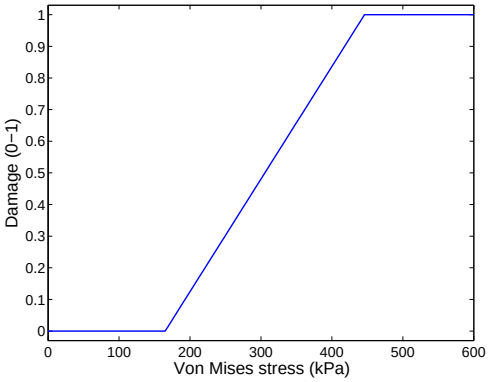

Fig. 2: Initial damage as a function of von Mises stress in the arterial wall. In this work, the value selected for the inferior limit of the von Mises stress is 165 kPa, corresponding to three times the value of the physiological circumferential tension calculated by Laplace's law, for a given blood pressure of 100 mmHg (13.3 kPa). For the superior limit of the von Mises stress, a value of 446 kPa was chosen, based on the mean value of the ultimate tensile stresses (UTS) for the media layer in the circumferential direction reported by Holzapfel et al. [42].

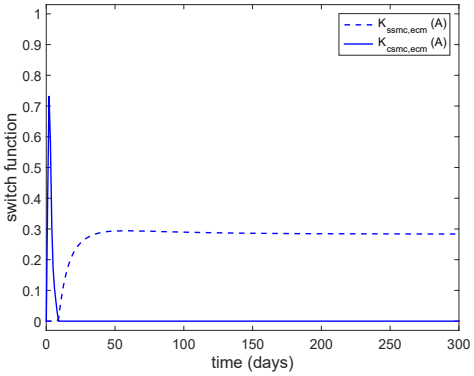

Fig. 3: Behaviour of the switch functions defined by Eqs. (8) and (9).

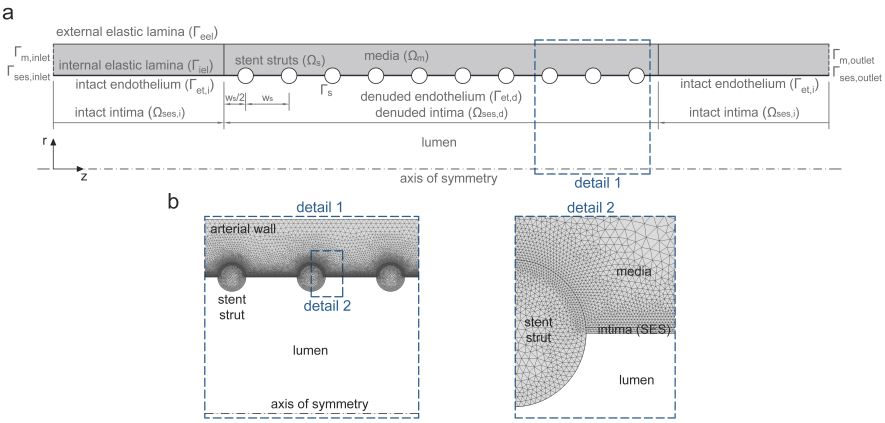

Fig. 4: (a) Baseline model geometry. The arterial wall is modeled as a multilayer structure distinguishing two different domains: intima and media layer. The adventitia is not modeled as a distinct layer but rather as a boundary condition at the outer surface of the media. The initial luminal radius, r_l, and the thickness of each wall layer, δ_j, in the unloaded geometry of the vessel are listed in Table 1, based on typical physiological values found in the literature. The stent implanted in the arterial wall is represented by 10 circular struts each of 0.125 mm radius, r_s, half-embedded in the tissue and located 0.7 mm centre-to-centre distance, w_s, simulating a small lesion of 7 mm. We note that the problem is actually symmetrical about the r-axis, i.e. half way between the 5th and 6th struts. (b) Details of the finite element (FE) mesh of the computational model.

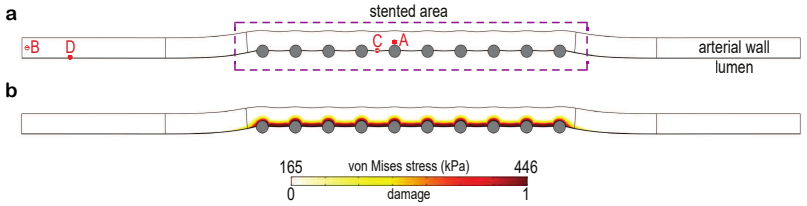

Fig. 5: (a) Deformed computational geometry and (b) von Mises stress distribution and corresponding quatification of the initial damage in the arterial wall. Points A and C are located close to a central stent strut in the media and in the denuded SES between struts, respectively. Points B and D are situated far away from the stented area in the media and SES, respectively.

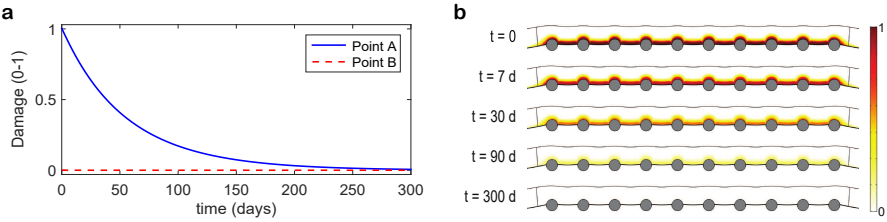

Fig. 6: Local evolution of the damage over time at two different points within the media (a) and distribution of damage in the stented area of the arterial wall at five different times after stent implantation (b). Point A and point B are located close to a central stent strut and far away from the effect of the stent in the media, respectively.

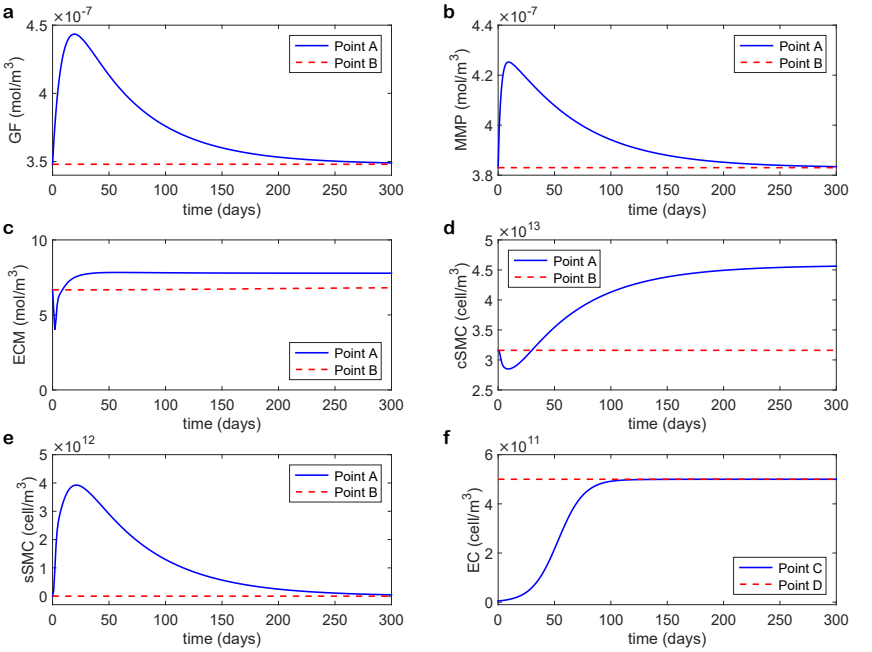

Fig. 7: Time-varying local concentration/density profiles of (a) GFs, (b) MMPs, (c) ECM, (d) contractile SMCs, (e) synthetic SMCs and (f) ECs at two different points within the arterial wall. Points A and C are located close to a central stent strut in the media and in the denuded SES between struts, respectively. Points B and D are situated far away from the stented area in the media and SES, respectively.

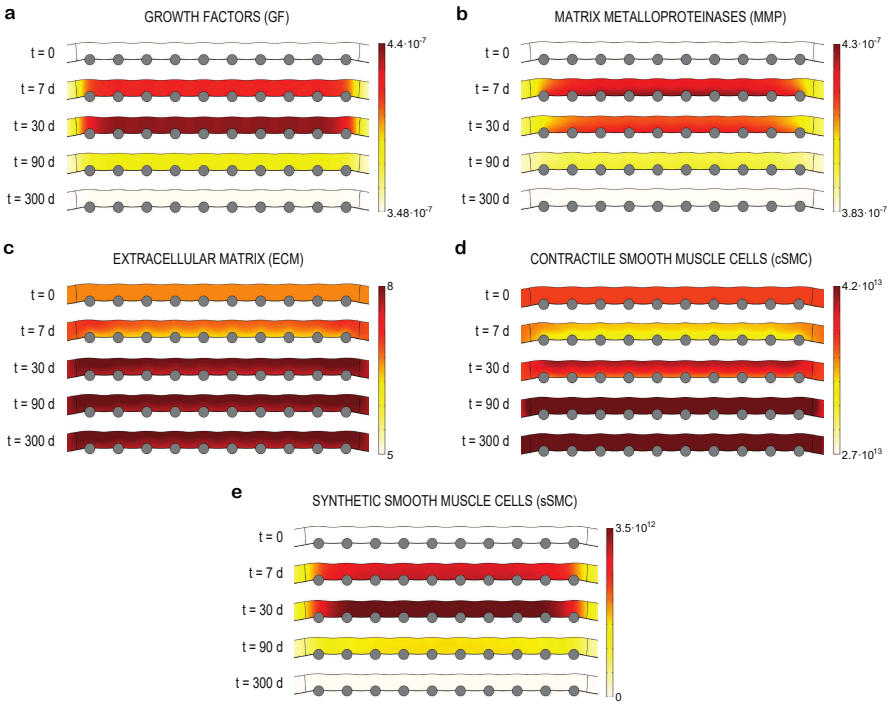

Fig. 8: Evolution of the distribution of all biological species in the media layer of the arterial wall at different times of the simulation. The substances concentration and cells density are shown in mol·m^{-3} and cell·m^{-3}, respectively.

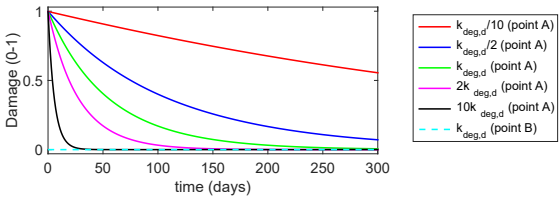

Fig. 9: Influence of varying damage degradation rate on the evolution of the damage. Please refer to the online Supplementary Material for a discussion.

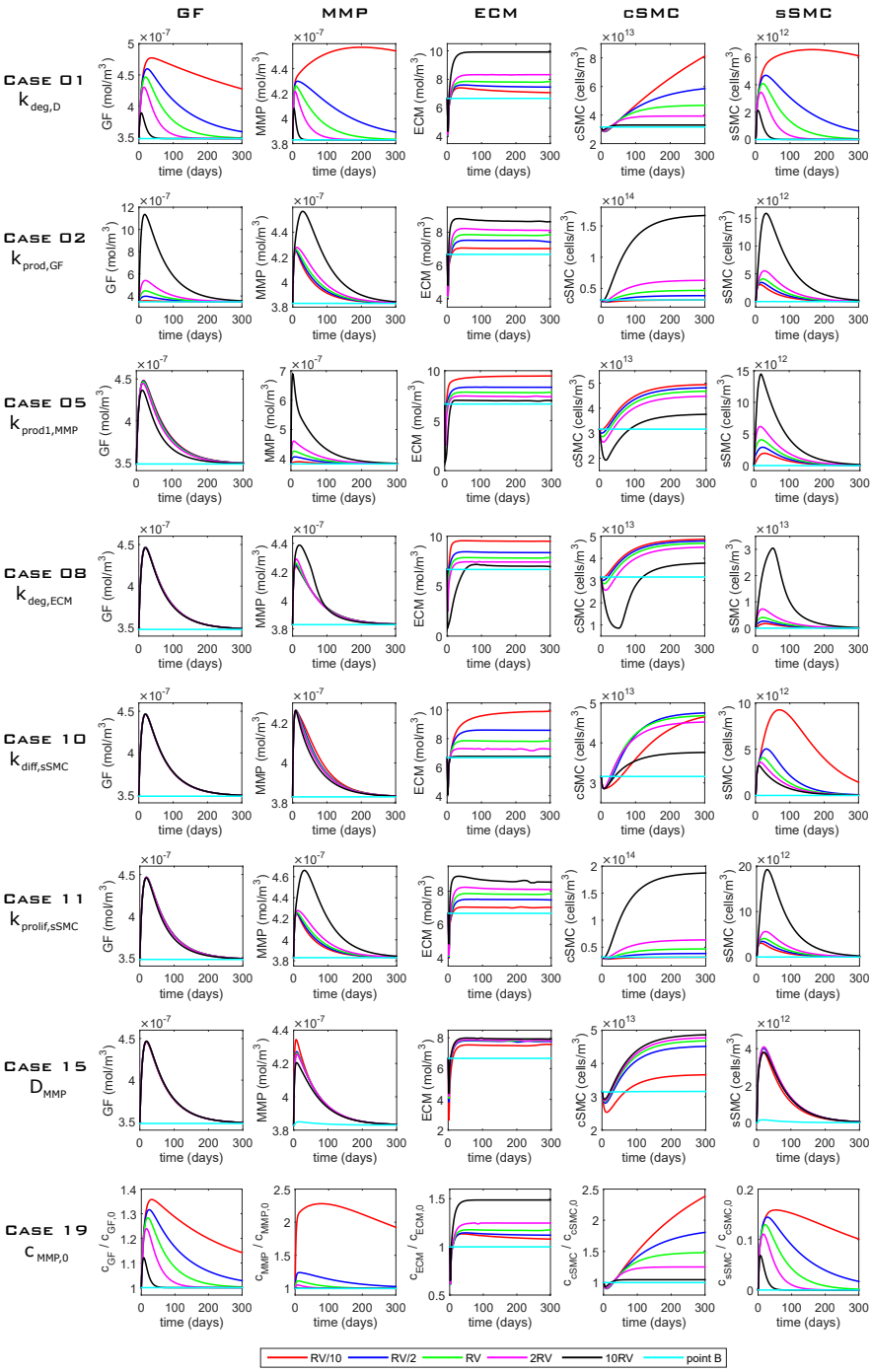

Fig. 10: Key results from the sensitivity analysis. The plots show the effect of varying several parameters on the concentration of GFs, MMPs and ECM as well as the density of contractile and synthetic SMCs for 8 different cases. Computations were carried out for four different values for each parameter apart from the reference value, RV, which is shown in Table 3. The values of 2RV and RV/2 were considered $\pm$ half the RV of the selected parameter; 10RV and RV/10 were given by increasing and decreasing by one order of magnitude the RV (see Table 4). The results shown for point B correspond exclusively to the RV (baseline model). Please refer to the online Supplementary Material for a discussion.

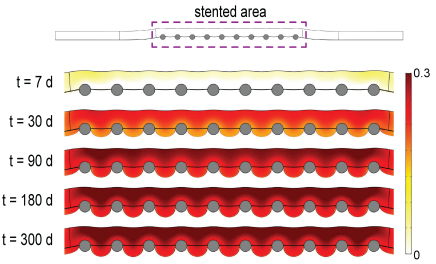

Fig. 11: Evolution of the volumetric growth at different times of the simulation for the baseline model.

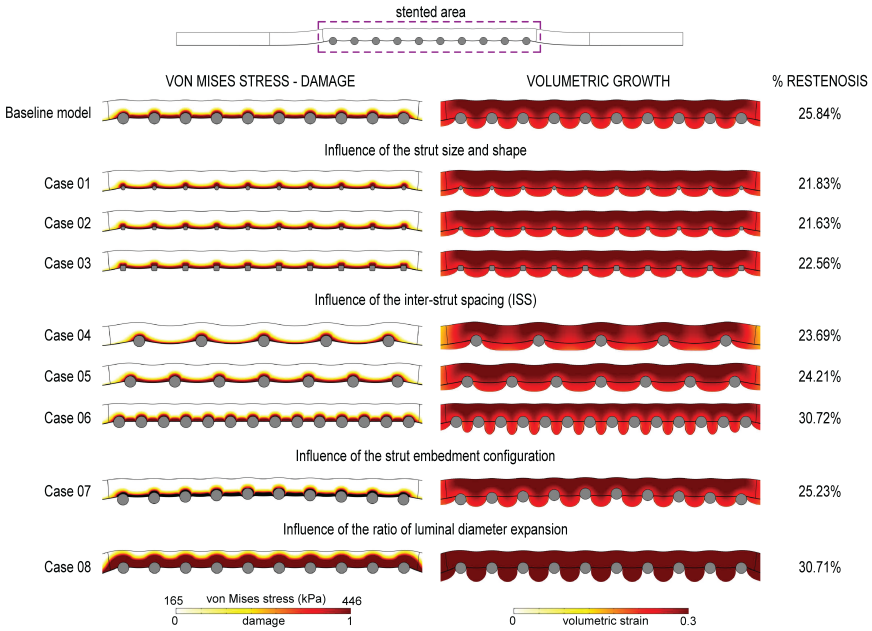

Fig. 12: The impact of different geometric configurations (Table 2) on Von Mises stress distribution and volumetric growth after 300 days.